Institution of MECHANICAL ENGINEERS

Journal of **MECHANICAL ENGINEERING SCIENCE**

Robust $\mathcal{H}_\infty$-based control of ARAS-diamond: A vitrectomy eye surgery robot

Abbas Bataleblu, Rohollah Khorrambakht and Hamid D Taghirad

Abstract

In this paper, we investigate the challenges of controlling the ARAS-Diamond robot for robotic-assisted eye surgery. To eliminate the system's inherent uncertainty effects on its performance, a cascade architecture control structure is proposed in this paper. For the inner loop of this structure, two different robust controls, namely, $\mathcal{H}_\infty$ and μ-synthesis, with stability and performance analysis, are synthesized. The outer loop of the structure, on the other hand, controls the orientation of the surgical instrument using a well-tuned PD controller. The stability of the system as a whole, considering both inner and outer loop controllers, is analyzed in detail. Furthermore, implementation results on the real robot are presented to illustrate the effectiveness of the proposed control structure compared to that of conventional controller designs in the presence of inherent uncertainties of the system and external disturbances, and it is observed that using $\mathcal{H}_\infty$ controller in the inner loop has superior robust performance.

Introduction

Using minimally invasive surgeries (MIS) has become very popular in advanced medical operations, and it has plenty of advantages for both surgeons and patients. This type of surgical operation is carried out through tiny incisions, and therefore, patients suffer reduced levels of trauma, blood loss, and pain. In MIS, there are smaller scars and shorter recovery time and hospital-stays.[1–4] Today, minimally invasive eye surgeries (MIES) have the same popularity, specially Vitreoretinal microsurgery, which is among the most technically challenging surgeries.[5] Eye surgeons work with limitations. Their work demands many years of training and the highest level of hand-eye coordination in order to ensure a safe surgery. Thus, to make full advantage of MIES during the surgery, minimum interaction force must be applied at the span of the sclera. Therefore, to perform eye surgery using MIS, remote center of motion (RCM) mechanisms are recommended. Hence, in performing the most challenging surgical tasks, RCM mechanisms significantly assist eye surgeon hand operations. There are several works that by providing the RCM, addressed robot-assisted ophthalmic surgery.[6–11] Currently, the RCM can be achieved by controlling redundant joints, adding passive joints, or using a mechanically constrained mechanism. However, for safety reasons using gravity compensation mechanisms, such as the one presented in EYE-RHAS manipulator[12] or,[4] is recommended. Most manipulators known as robotic-assisted minimally invasive eye surgery, provide tilt and pan angles about the pivoting point besides one other degree of freedom along the tool axis.[13–17]

The RCM may be achieved using various mechanisms, some of them are reported in literature.[18–26] Researchers mostly use these RCM mechanisms for developing robotics systems for robotic-assisted surgery and surgery training applications. The ARAS-Diamond robot considered in this paper is based on a different methodology called the spherical parallel

Advanced Robotics and Automated Systems (ARAS), Industrial Control Center of Excellence (ICCE), Faculty of Electrical and Computer Engineering, K.N. Toosi University of Technology, Tehran, Iran

Corresponding author:
Hamid D Taghirad, Advanced Robotics and Automated Systems (ARAS), Industrial Control Center of Excellence (ICCE), Faculty of Electrical and Computer Engineering, K.N. Toosi University of Technology, 16315-1355 Tehran, Iran.
Email: taghirad@kntu.ac.ir

mechanism to mechanically generate the RCM point.[27] This robot is designed to perform as the slave robot in a robotic-assisted eye telesurgery system in which the surgeon operates on a master haptic console to send desired commands to this slave robot.[28–30] However, for the sake of brevity, details of the robot design are omitted in this paper. The workspace of this robot is a hemisphere, and all joint axes intersect at the RCM point. As it is shown in Figure 1, this parallel robot provides two degrees of rotational motion and one degree of transmission motion, which is totally qualified for eye surgery. Owing to the parallel structure of the robot, higher structural stiffness, and improved position accuracy is obtained compared to that of other existing mechanisms, which makes it more appropriate for precise motions such as in eye surgeries. To provide a back-drivable transmission mechanism with high accuracy and zero backlashes, the manipulator utilizes two capstan drives for both actuators that provide rotational motions. Kinematics formulation and the structure of the robot are presented in Molaei et al.,[31] and the dynamic formulation of the manipulator may be achieved similar to what reported in Danaei et al.[32] In this robot, actuators are selected after simulating the mathematical model of the robot using CAD parameters to calculate the required torques of each actuator. Furthermore, encoders are chosen so as the accuracy of about 100×10^{-6} in the workspace is easily achievable. However, to satisfy clinical deployability and safety features, further modification is needed to be considered on the robot.

Using robots for eye surgery necessitates very precise motion in a small workspace. Therefore, it is pivotal for the robot to be precise in design and control. However, there are a variety of uncertainties in kinematic parameters and unmodeled dynamics besides external disturbances and noise, which make conventional controllers incapable of providing the required performance in trajectory tracking for eye surgery applications. Hence, designing a robust

Figure 1. ARAS-Diamond robot: the novel 2RT spherical parallel robot for eye telesurgery.

control structure is essential to lessen these uncertainties effects.

Although common linear-based controllers such as PID and Linear Quadratic Regulator (LQR) have simple designs, since they are based on a linearized model, the nonlinear behavior of the system has been neglected in these controllers structure. Thus, the designed controller does guarantee the stability and the performance of the real system just near the operating point, and its performance is not uniform at different configurations, and in the presence of measurement noise and external disturbances. On the other hand, nonlinear-based controllers such as sliding mode, adaptive, and Lyapunov-based controllers consider uncertainties and constraints in the nonlinear model of the actual system.[33] Therefore, the accurate nonlinear dynamic model is required, which is generally difficult to obtain. In addition, if a controller is designed for a non-minimum phase (NMP) system, its closed-loop internal stability becomes prominent. Hence, in this paper, it is proposed to use control strategies like linear robust controllers to analyze robust stability and performance of the closed-loop system altogether, for real-world implementations.

Several successful linear robust controllers have been proposed in the literature to mitigate kinematics and dynamics uncertainties effects on linear-based controllers.[34–36] A robustness study among a modified fractional order proportional plus integral and derivative (FOPID) versus $\mathcal{H}_\infty$ and μ-synthesis controllers is reported in Seyedtabaii.[37] In Bataleblu et al.,[38] a robust $\mathcal{H}_\infty$ controller was simulated in the presence of modeling uncertainty and actuator saturation without implementation results. Decentralized robust control for teleoperated needle insertion is reported in Agand et al.[39] A parametric robust approach PID control for a laparoscopic surgery robot is designed in Bolea[40] and robust $\mathcal{H}_\infty$ control of a tendon–driven elastic continuum mechanism is reported in Shu et al.[41] Furthermore, $\mathcal{H}_\infty$-based control of a quadrotor attitude is presented in Noormohammadi Asl et al.[42]

The main contribution of this paper is the design and implementation of a robust $\mathcal{H}_\infty$-based controller for the 2RT spherical parallel manipulator in hand in the presence of unstructured uncertainties and external disturbances. Hence, in the controller synthesis, the control design objective is robust stability assurance in the presence of uncertainty and disturbance in addition to suitable trajectory tracking performance. For this aim, using system identification based on the experimental frequency response estimates, the coupled and nonlinear dynamics of the robot are encapsulated by a linear model in addition to a multiplicative uncertainty block. This system identification is performed on the velocity loop, such that by using the linear model and mixed sensitivity formulation, two $\mathcal{H}_\infty$ and μ-synthesis controllers be designed
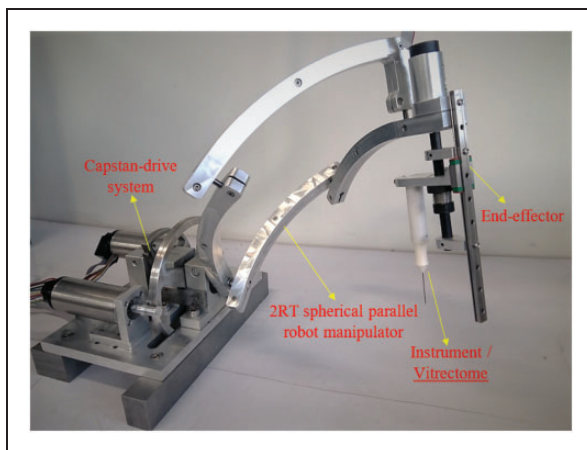
for the inner loop of a cascade structure. Next, these two controllers are compared in terms of their robustness and performance and implemented on the robot. Then, using forward kinematics to derive the orientation of the surgery tool in spherical coordinates, a PD controller is designed for the outer loop, and the robust stability of the whole closed–loop system is analyzed by using μ-analysis.

The remainder of the paper is organized as follows. The uncertainty block and linear model encapsulation of the robot are described in the next section. Section three represents $\mathcal{H}_\infty$ control design for the robot in the presence of multiplicative uncertainty. The controller design based on μ-synthesis is reported in Section four. Section five provides the comparative study of the two designed controllers and μ–analysis of the outer loop of the proposed cascade structure. The experimental setup and implementation results are described in section six, and finally, the concluding remarks are declared in the last section.

Uncertainty and linear model encapsulation

This section of the article aims to apply $\mathcal{H}_\infty$ synthesis to the robot. For this means, a linear model encapsulated with multiplicative uncertainty is obtained from the nonlinear dynamics of the true system. For this purpose, using practical experiments and with the help of system identification based on the experimental frequency response estimates on the experimental data, the linear model may be achieved in a systematic way. In systems with dominant nonlinear behavior such as parallel robots, nonetheless, this might not perform efficiently. Consequently, the encapsulated linear model will result in a high profile of uncertainty. Moreover, the 2RT spherical parallel robot in hand is an inherently unstable multi-input multi-output (MIMO) system which necessitates closed–loop experiments for the purpose of identification.

Accordingly, for the robot to have a more linear and stable performance, closed-loop feedback by the use of an Inverse Dynamics Control (IDC) with a PD controller is proposed. The IDC attenuated the nonlinear and coupling behavior of the robot manipulator. However, it requires the dynamic formulation of the robot alongside its kinematics and dynamics parameters to generate IDC terms. To not rely on the dynamic formulation and all kinematics and dynamics parameters, Partial Linearization IDC is recommended in this paper. Therefore, just the configuration dependent gravity term G of the robot is demanded to be compensated.[43] Hence, it suffices to just apply a very slow trajectory with almost zero velocity and acceleration at any configuration in the workspace to the robot manipulator, such that the generated torque estimates the required gravitational term.

Gravitational term identification

Figure 2 depicts the structure of the 2RT spherical parallel robot in which, rotation of the active joints of the mechanism is about AO, and it is measured with respect to ZX plane about Z axis that is shown by θ_1 and θ_2 for each active joint, respectively. Furthermore, any point of the mechanism moves on the surface of a sphere for any input angles, and a spherical coordinate expresses its position. The orientation of the surgery instrument in spherical coordinates is considered through γ and ϕ in which γ is rotation of OD about the X axis, while ϕ is rotation of AD arc about Z axis and it is measured with respect to ZX plane.[31]

The achievable workspace for eye surgery provided by this mechanism is about $\pm45^\circ$ for ϕ and 45° for γ. Furthermore, if we represent the circular length of proximal and distal links of the mechanism by α and β, the robot workspace can be shown as Figure 3. In the design of the 2RT robot in hand, both these circular lengths are set to 45°. Accordingly, this robot is completely singular free in its sphere workspace, a stringent requirement for any eye surgery operation. Therefore, it is adequate that the identifying trajectory for the gravitational term lies within this workspace, and furthermore, to sweep the whole region needed for eye surgery operation. This trajectory for both γ and ϕ is depicted in Figure 4. For black-box identification of G term, this trajectory is converted to the joint space using inverse kinematics to be used for joint-based feedbacks on the motors.

For the sake of gravity term identification, and by the implementation of a closed-loop trajectory tracking control scheme, this desired trajectory is applied to the robot, and time-domain data of the actual orientation of motors and the torque generated by the controller is acquired for black-box system identification. To approximate the intricate connection between a set of inputs and outputs, a variety of machine learning methods such as artificial neural
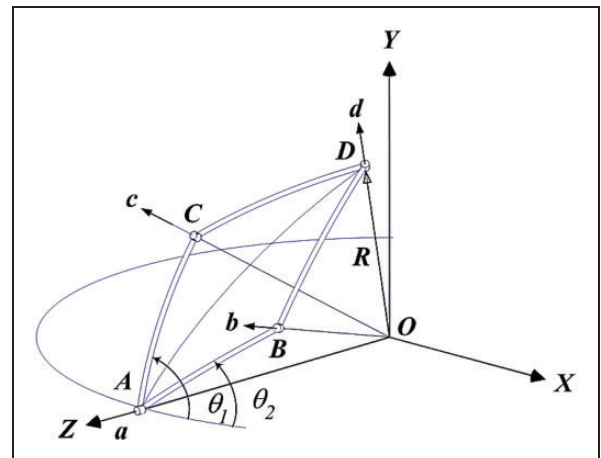

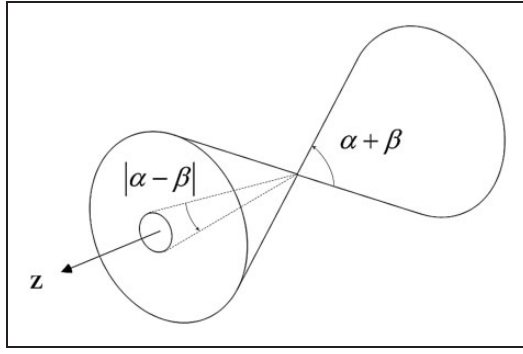**Figure 2.** Structure of the 2RT spherical parallel robot.[31]

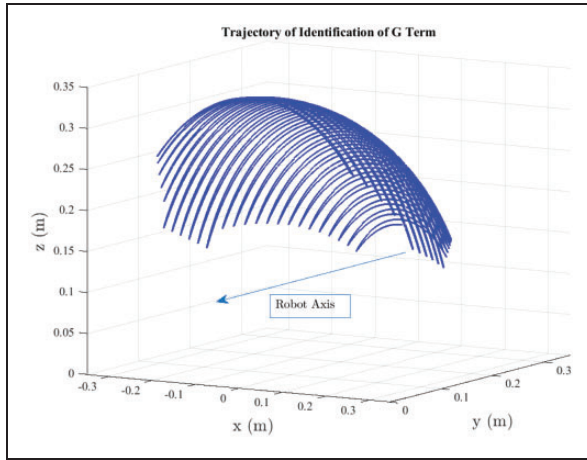**Figure 3.** General workspace of the mechanism.[31]

Figure 4. Desired trajectory for the gravitational term identification.

networks (ANNs) have been proposed in the literature and may be used for G term identification. In this paper, two layers ANN with fifteen neurons in the first layer and two in the other one is used. After training the network by using the Levenberg-Marquart algorithm, its performance reached a Mean Squared Error (MSE) value of 0.0015, using equation (1), which is quite suitable for our purpose. In the next step, to find if our network is well trained, just the G term is used in the feedback loop. The closed-loop result shows that the robot acts completely gravity-free, and it can stay at any desired configuration. Consequently, the ultimate Partial Linearization IDC control scheme is implemented, as depicted in Figure 5.

$$MSE = \frac{1}{n} \sum_{i=1}^{n} (y_i - \hat{y}_i)^2 \qquad (1)$$

Linear model identification

After identifying the gravity term, we aim to identify a MIMO black-box system based on inputs and outputs experimental data for the purpose of $\mathcal{H}_\infty$ controller synthesis. Thus, a frequency-domain
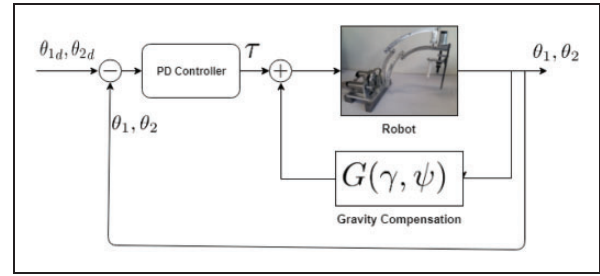
Figure 5. Partial Linearization IDC control scheme.

identification approach is performed, such that a linear continuous-time model is obtained. In this method, using the control strategy proposed in Figure 5, a random signal is implemented on both active joints of the robot as an exciting input. During this experiment, this signal is applied in 23 different configurations of the robot workspace needed for eye surgery. After performing these experiments for our MIMO system, a linear transfer matrix is estimated for each experiment to suitably model the input-output behavior.

In order to identify the MIMO system, different input-output pairs could be considered. For the purpose of controller synthesis, it is essential to use torques inputs to the system as the inputs data for our black-box system, while either position or velocity of the robot joints as the outputs. Both cases were examined, and it is observed that the latter case where the angular velocities are considered as the outputs of the transfer matrix identification will provide better fitness. This is due to the fact that there is an intrinsic integrator in the position outputs of the system, which might induce some non-vanishing bias in the output because of unmodelled nonlinear dynamics.

Consequently, we propose to use the robust controller in the inner loop of the cascade architecture using this linear model of the system, while a simple PD controller is used in the outer loop to attenuate the nonlinear dynamics while preserving the position trajectory tracking objective in the structure. By using the linear model and mixed sensitivity formulation, two $\mathcal{H}_\infty$ and μ-synthesis controllers are designed for the inner loop of a cascade structure as detailed in the next sections.

In order to identify a continuous-time transfer matrix, MATLAB identification toolbox is used, while selecting a proper set of poles and zeros is essential. Nonetheless, note that transfer functions to be identified are considered low order to have a less complicated $\mathcal{H}_\infty$-based controller derived. The simplest structure for the linear model of the system would be a first-order system for velocity outputs. Therefore, one zero and one pole for each identification subsystem is considered, and as a result, 23 different two-input two-output first-order models have been identified, whose singular values are shown in
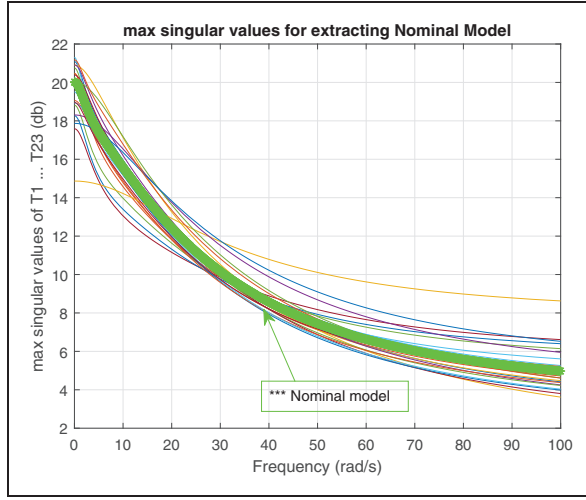
Figure 6. Singular values plot of 23 first order uncertain models of the experiments.

Figure 6. It is observed that all these uncertain models are stable but non-minimum phase.

From Figure 6, one may conclude that the behaviors of all 23 transfer matrices in different configurations of the robot operating points are quite close. This is the result of the proper choice of feedback linearization and input-output selection in the identification process. Among all these uncertain models, one which is operated in the middle of the robot workspace, and is nearly the median of all responses, is selected as the system nominal model. This nominal model is depicted in green star-line in Figure 6, and its transfer matrix is given as follows:

$$
G_0 = \begin{bmatrix} \dfrac{-1.0114(s - 86.14)}{(s + 16.67)} & \dfrac{-0.4705(s - 18.46)}{(s + 2.202)} \\ \dfrac{-0.29947(s - 34.66)}{(s + 3.186)} & \dfrac{-1.2048(s - 74.47)}{(s + 12.29)} \end{bmatrix}
$$
$$(2)$$

Uncertainty encapsulation

Having the nominal model identified through experiments, the next step is to encapsulate the system uncertainty using a full block of multiplicative uncertainty. For this type of uncertainty encapsulation, the uncertain system denoted by G_{un} is related to the nominal model G_0 by

$$
G_{un} = (1 + \triangle W_{un})G_0 \tag{3}
$$

in which, $\triangle$ denotes a permissible and normalized uncertainty block, where $(\|\triangle\|_\infty < 1)$, and W_{un} denotes the uncertainty weighting function. By this representation, the uncertainty profile may be easily derived by:

$$
\left| \frac{G_{un}(j\omega)}{G_0(j\omega)} - 1 \right| < |W_{un}(j\omega)|, \quad \forall \omega \tag{4}
$$
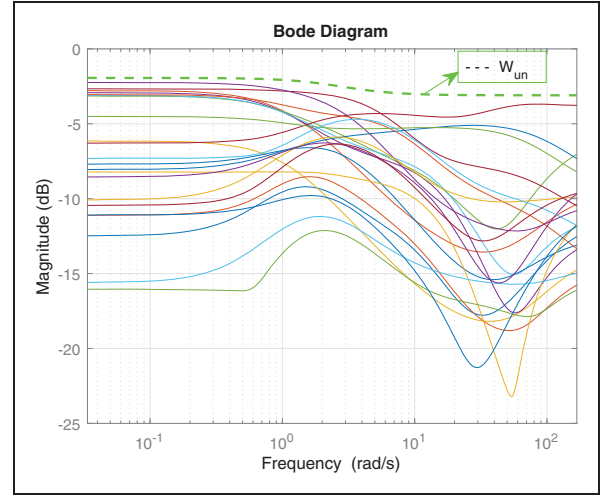
Figure 7. Multiplicative uncertainty profiles.

The uncertainty profiles are derived for all the experiments and shown in Figure 7 through equation (4). The uncertainty weighting matrix W_{un} may be determined by the least upper bound of these uncertainty profiles, which is depicted by the dashed green line in Figure 7. A numeric estimate of such uncertainty profile may be given as:

$$
W_{un} = \begin{bmatrix} \dfrac{0.7(s + 3)}{(s + 2.625)} & 0 \\ 0 & \dfrac{0.7(s + 3)}{(s + 2.625)} \end{bmatrix} \tag{5}
$$

Robust $\mathcal{H}_\infty$ controller design

In the presence of uncertainties in the robot manipulator and external disturbances, the designed controller should guarantee robust stability while inducing suitable tracking performance. Using mixed-sensitivity problem as depicted in Figure 8, these objectives can be well reduced to equation (6), in which S is the sensitivity function, T denotes the complementary sensitivity function, and U is the control effort transfer function. Furthermore, for a multiplicative uncertainty representation, W_s is the performance weighting matrix, while suitable tracking performance may achieve by enforcing $\|W_s S\|_\infty < 1$. Furthermore, W_{un} is the uncertainty weighting matrix, and $\|W_{un} T\|_\infty < 1$ is the result of the small gain theorem to enforce robust stability. Moreover, $\|W_u U\|_\infty < 1$ requires bounded control effort through proper assignment of W_u, the control effort weighting matrix.

$$
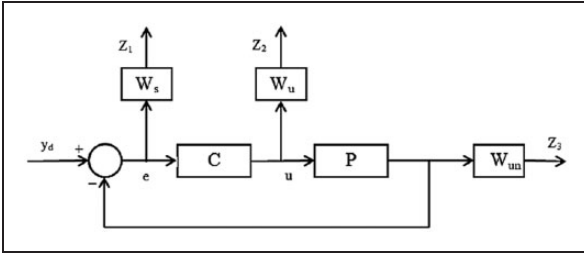\|T_{zyd}\|_\infty = \left\| \begin{matrix} W_s S \\ W_u U \\ W_{un} T \end{matrix} \right\|_\infty < 1 \tag{6}
$$

Figure 8. Block diagram representation of a generalized regulator problem in $\mathcal{H}_\infty$ framework.

While the performance weighting matrix can be selected using the desired input-output behavior of the robot angular velocity, W_u may be assumed as a constant function $W_u(s) = \alpha$ to bound the control inputs at all frequencies. In order to properly set the performance weighting matrix W_s, it is assumed the desired system response is as a standard second-order transfer function with a settling time less than 0.6 seconds and a desired overshoot less than %10. Hence, from $\frac{4.6}{\zeta\omega_n} < 1$ and $exp(\frac{-\zeta\pi}{\sqrt{1-\zeta^2}}) < 0.1$, we can obtain $\zeta = 0.85$ and $\omega_n = 10/, rad/s$. Therefore, W_s can be achieved from the inverse of the desired sensitivity function as follows:

$$T_{id} = \frac{100}{s^2 + 17s + 100} \tag{7}$$

$$W_s < \frac{1}{S_{id}} = \frac{1}{1 - T_{id}} = \frac{s^2 + 17s + 100}{s(s + 17)} \tag{8}$$

In order to make W_s a stable weighting function and strictly proper, we add a far and non-dominant pole to it and slightly transfer the pole at the origin. Moreover, to tune the performance in the design procedure of the controller, a coefficient a is considered for the final form of the W_s:

$$W_s = a \frac{s^2 + 17s + 100}{(s + 0.001)(s + 17)(0.001s + 1)} \tag{9}$$

The design procedure for adjusting the control effort design parameter α, and the performance parameter a is iterative. In order to solve the mixed sensitivity problem, the robust toolbox of matlab[a] is used. Consequently, after some iterations, the final obtained value for W_u and W_s are as following:
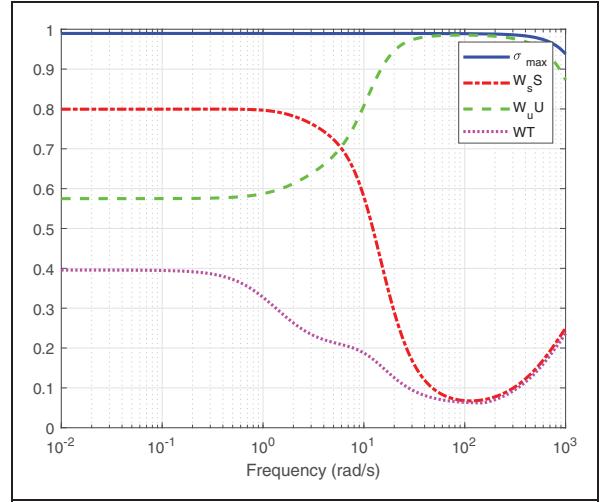

Figure 9. The closed loop system singular values and frequency response.

$$W_u = \begin{bmatrix} 1 & 0 \\ 0 & 1 \end{bmatrix} \tag{11}$$

Optimal performance index of the $\mathcal{H}_\infty$ designed controller reached $\gamma_{opt} = 0.9895$ to optimally solve the mixed sensitivity problem. Figure 9 depicts the singular value plot of the system. As it is shown in this figure, the solid blue line is the maximum singular value of the final closed-loop system which its maximum value is less than one, and it is quite flat for a large frequency range. The bode diagram of the WT transfer function is depicted by the dotted purple curve, whose maximum value is smaller than 0.4. As a result, the closed-loop system is robustly stabilized. Furthermore, the dashed green curve depicts the control effort frequency content, which is small at low frequencies, while, as expected, it is increasing at higher frequencies, while its infinity norm is less than one. Finally, W_sS is plotted by the dash-dotted red line. This curve shows the performance transfer function, which is close to one at low frequency and the controller bandwidth. This frequency analysis indicates that the designed controller preserves robust stability in the presence of actuator limitations while providing satisfactory trajectory tracking performance.

μ- synthesis controller design

As it is elaborated in the previous section, the robust $\mathcal{H}_\infty$ controller designed has an iterative nature, and to reach

$$W_s = \begin{bmatrix} \dfrac{0.94(s^2 + 17s + 100))}{(s + 0.01)(s + 17)(0.001s + 1)} & 0 \\ 0 & \dfrac{0.94(s^2 + 17s + 100))}{(s + 0.01)(s + 17)(0.001s + 1)} \end{bmatrix} \tag{10}$$

the suitable controller, special skills in the frequency domain for the experienced designer is needed. In order to automate these iterations, μ-synthesis controllers are proposed in the literature. In this controller design framework, linear fractional transformations representation is used to define the optimization problem. As it is depicted in Figure 10, while a lower Linear Fractional Transformation (LFT) represents the controller, the uncertainty block shall be extracted as an upper LFT. In this figure, M introduces the generalized plant transfer matrix. Therefore, alongside the robust

$$W_s = \begin{bmatrix} \dfrac{0.6(s^2 + 17s + 100))}{(s + 0.01)(s + 17)(0.001s + 1)} & 0 \\ 0 & \dfrac{0.6(s^2 + 17s + 100))}{(s + 0.01)(s + 17)(0.001s + 1)} \end{bmatrix} \tag{15}$$

stability in the optimization problem, the demand for performance is also considered as the upper LFT. Such a problem may be written as follows in terms of LFT's:

$$\{F_u(M, \triangle) : \triangle \in \triangle, \max_\omega[\triangle(j\omega)] \leq 1\} \tag{12}$$

In which, $\triangle$ denotes all stable and permissible uncertainties that their infinity norm is smaller than one. In μ-synthesis, the target of designing the controller is to find a stabilizing controller K such that for all $\triangle \in \triangle$, the infinity norm of the closed-loop system transfer matrix is minimized. This can be interpreted as minimizing the following lower LFT:

$$\min_\gamma \|F_l[F_u(M, \triangle), K]\|_\infty < 1 \tag{13}$$

This objective may be achieved by calculating the structural singular value of the system as follows:[38]

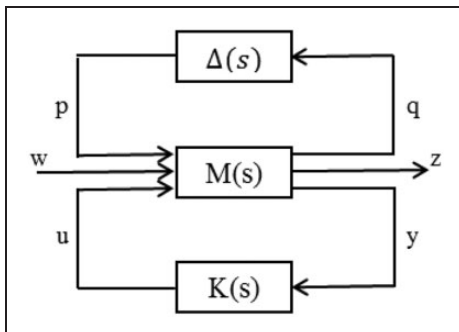$$\max_\omega \mu_\triangle(F_l(M, K)(j\omega)) < 1 \tag{14}$$

For solving this optimization problem iteratively, usually, the robust toolbox of matlab[b] is used. Obtaining high order controllers is the only drawback of this method, which is due to the nature of solving this optimization problem. In order to design the controller for our problem in hand, the same weighting function as what given in $\mathcal{H}_\infty$ design procedure is considered for the performance. However, the adjusting coefficients α and a is set differently. Consequently, after some correction steps, the final value obtained for W_u and W_s are as following:

$$W_u = \begin{bmatrix} 0.56 & 0 \\ 0 & 0.1 \end{bmatrix} \tag{16}$$

The procedure to design the controller has used five iterations, while the structured singular value is reduced from 1.139 to 0.998. The order of the final designed controller is 16, and in order to reduce the controller, its Hankel norm is plotted in Figure 11. It is seen in this figure that only the five first singular values are significant, and therefore, the controller truncation is based on the fifth-order controller.

Controllers comparison and overall system μ analysis

After designing two robust controllers in the velocity loop as it is illustrated in Figure 12, the performance
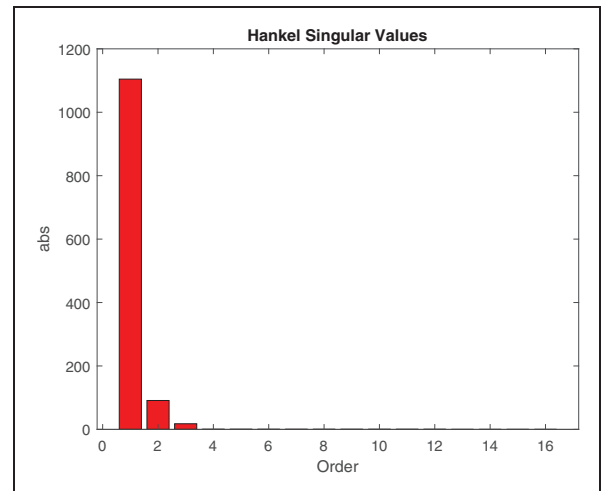

Figure 10. Standard representation of $\triangle - M - K$.

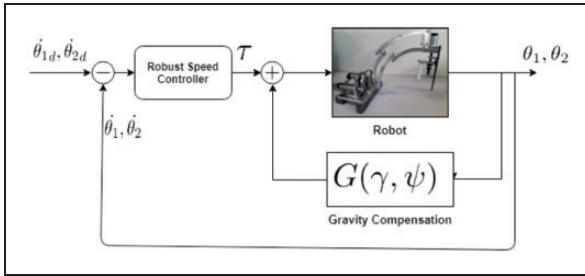**Figure 11.** Hankel norm plot of the μ-synthesis controller.

Figure 12. Robust controller in the angular velocity loop feedback.

Figure 13. Robust stability analysis of designed controllers.
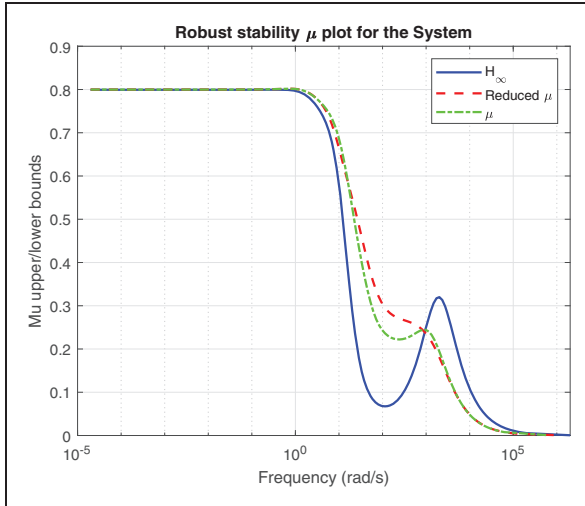

Figure 14. Robust performance analysis of designed controllers.

of them is compared quantitatively in terms of robust stability and performance in this section. For this purpose, the structured singular values for both controllers are determined, and their robust stability and performance are depicted in Figures 13 and 14 respectively. As it is shown in Figure 13, all three controllers meet the robust stability criterion for all frequencies, and their structural singular values are smaller than 1. Furthermore, from Figure 14, one may conclude that both μ and $\mathcal{H}_\infty$ controllers perform robustly at all frequencies. Nonetheless, the reduced form of the μ-synthesis controller's structured singular value is more than one in mid-range frequencies, and it does not meet the robust performance criterion at all frequencies. In addition, the frequency response of the resulting controllers plotted in Figure 15 shows that all three controllers have a similar frequency pattern. However, the magnitude of $\mathcal{H}_\infty$ controller is less than that of μ-synthesis controller at low and mid frequencies. Therefore, the required control effort is lower, and it contains less oscillation. If the control effort is not of restriction, μ-synthesis would have less steady-state errors. However, since this controller is of a high order and its implementation and tuning on the real robot is more challenging, we propose implementing $\mathcal{H}_\infty$ controller in practice.
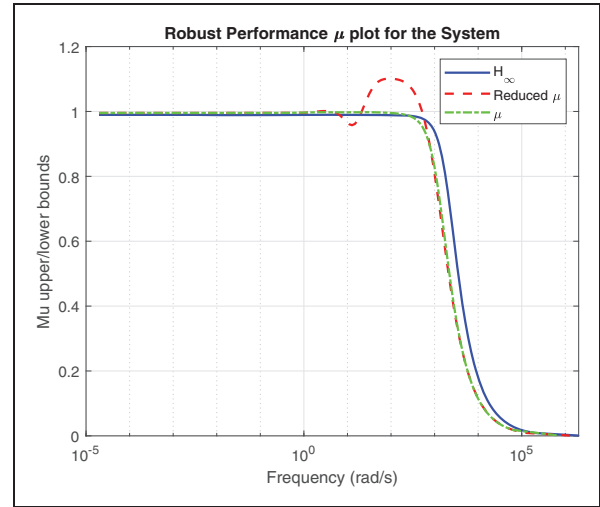
As we mentioned before, developed robust controllers are designed to be utilized in the inner loop of a cascade control structure. In order to have position tracking, an outer loop with at least a PD controller may be used in a cascade structure illustrated in Figure 16. It is proved that the inner loop of this structure is designed to be stable. Nevertheless, the overall system shall be robustly stable. In order to perform this analysis, the $\mathcal{H}_\infty$ controller, which shows superior performance in the presence of actuator saturation is only analyzed.

For this purpose, since the controller in the inner loop is well defined and the system is encapsulated with a linear model and multiplicative uncertainty, it is possible to form the whole uncertain closed-loop system for the known PD controller. Through an iterative way, the PD controller gains are tuned as following to ensure robust stability is preserved.

$$P = \begin{bmatrix} 35 & 0 \\ 0 & 90 \end{bmatrix}, D = \begin{bmatrix} 4 & 0 \\ 0 & 10 \end{bmatrix} \tag{17}$$

The structured singular values for the whole system is calculated for the augmented uncertain system, and the robust stability plot is depicted in Figure 17. As it is seen for the above tuned PD gains, the robust stability criterion of the whole system is satisfied for all frequencies, and its structural singular value is less than one.

Physical implementation

Experimental setup

In this section, we present the experimental setup. The robot itself is designed and implemented in the Advanced Robotic and Autonomous Systems (ARAS). The robot actuators are driven by a capstan-drive system shown in Figure 18. This system
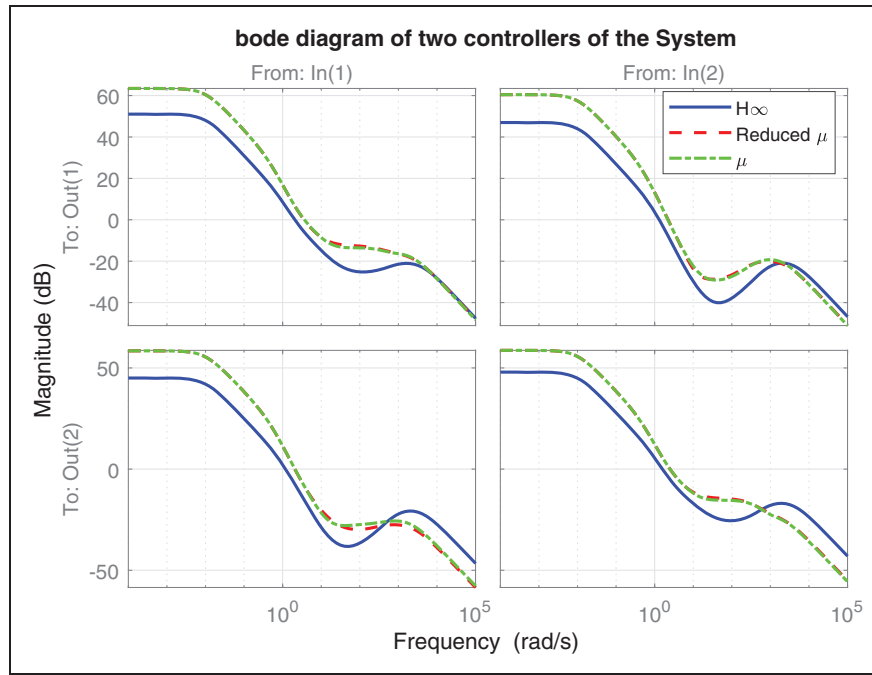
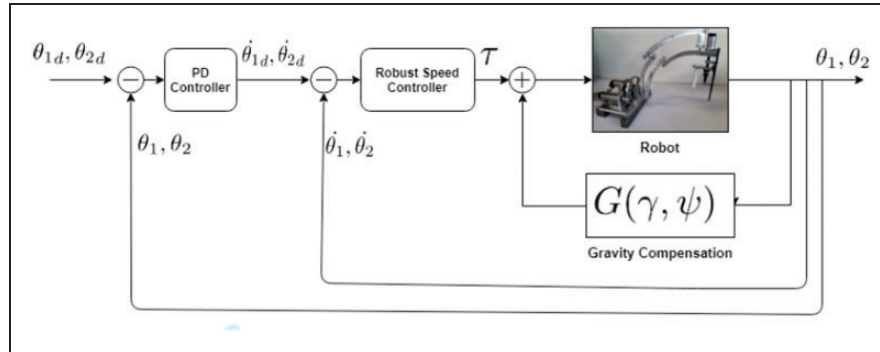**Figure 15.** Frequency response of resulting controllers.

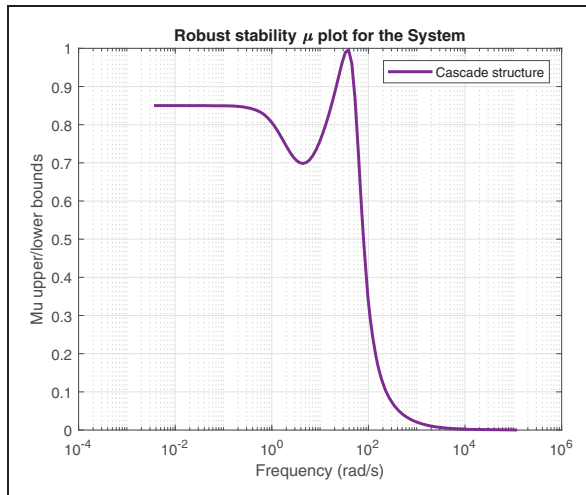**Figure 16.** Cascade control structure used for controlling robot manipulator.

Figure 17. Robust stability analysis of the system as a whole.

works with a 0.5*mm* diameter steel wire rope. The electronically commutated (EC) DC motors utilized in this system are MAXON EC-max 40 motors, which have the capacity to produce 120 watts of power. Furthermore, encoders used here to measure the angular position of the motors are HEDL 5540 with 500 pulses. In addition, to drive the motors, the Maxon EPOS2 50/5 controller has been used in this system.

The low-level control of the motors are handled by the specialized drivers set into their current control mode. In this mode, the drivers are responsible for performing the commutation and maintaining the required current which is linearly proportional to the required torque on the motor's shaft. For setting the reference current, we enabled the analog inputs of the drive. Through this interface, we can

command the system at the maximum possible frequency and with the lowest possible latency. Actuators installed on the robot alongside with their drivers are illustrated in Figure 19.

For implementing our control system, we utilize the Matlab Simulink Real-Time target. This system is built upon the Matlab Real-Time kernel, which is a lightweight and custom made Real-Time Operating System (RTOS) that can be generated within the Matlab software. This RTOS can booted on a conventional X86 PC, which is called the Target in Matlab terminology. It has support for many Data Acquisition (DAQ) Cards alongside standard interfaces such as UART and Ethernet. In this work, we have exploited the Real-Time UDP capability of this system for the exchange of data. The software for this system is generated on an independent host computer within the Simulink development environment of the MATLAB software. In this design, some individual blocks are responsible for reading sensors and setting control commands at a rate of one KHz. When the process of designing the controller is accomplished, it is automatically translated into C code, and after compilation, the executable binary is sent to the target PC through an independent Ethernet connection.

As we mentioned, the data exchange with the target system is achieved through the Ethernet connection and using UDP protocol. For this reason, we designed and built a custom DAQ system using an ARM Cortex-M4 STM32F4 discovery evaluation board with an Ethernet PHY. Our deployed controllers to the Simulink Real-Time target provide the current commands for the driver at a rate of one KHz. These commands are transferred to the microctorller through the UDP interface with a latency of less than 0.25 ms. The development board is connected to four DACs through SPI interfaces. After proper signal conditioning using simple op-amp circuits, the analog outputs of these DACs are connected to the analog interfaces of the motor drivers. This microcontroller is connected to the Target PC through its Ethernet PHY, and on the other hand, it is connected to the motor encoders for reading their angle and a set of DAC chips for providing analog outputs. It is important to note that this microcontroller-based DAQ system can provide deterministic timings due to its single thread software architecture dedicated to the task at hand. This DAQ system is illustrated in Figure 20. Furthermore, the overall system architecture is represented in Figure 21.
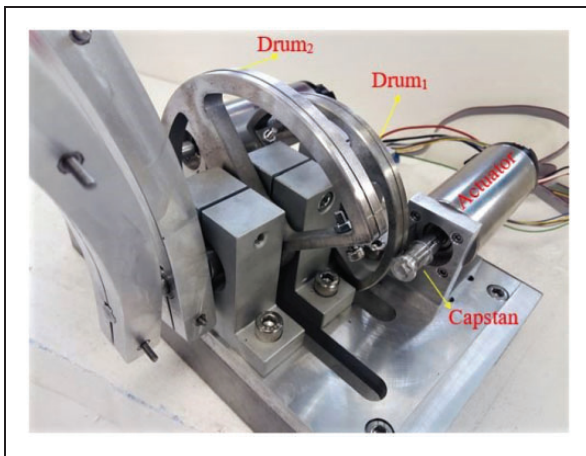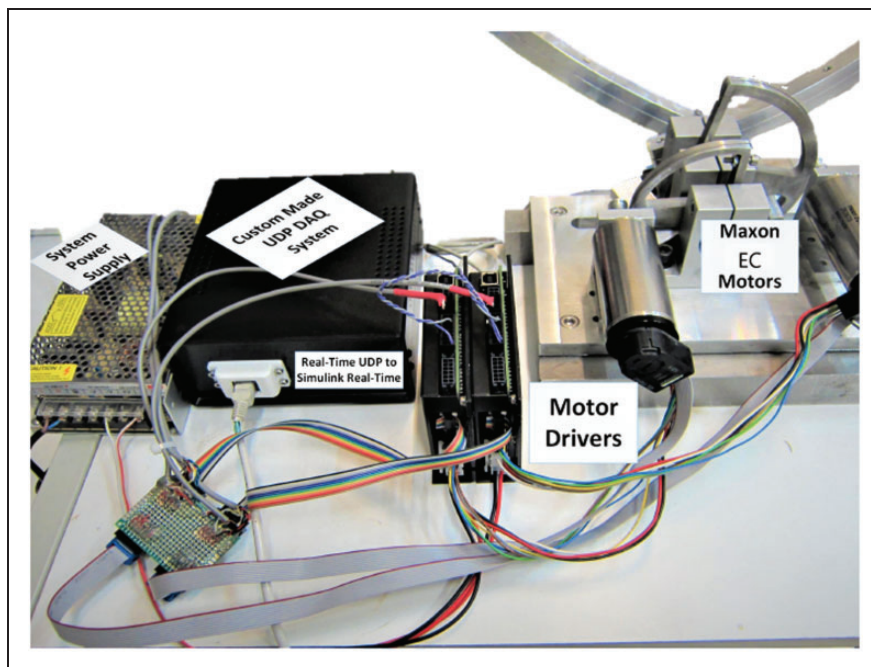

Figure 18. Capstan-drive system.

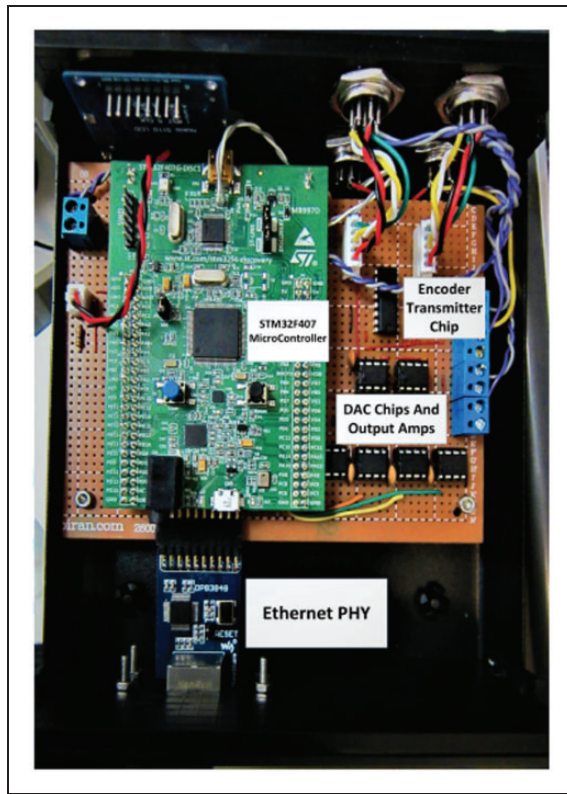**Figure 19.** The experimental setup.

Figure 20. The custom DAQ system with its constituent parts.

Experimental results

In this part, the performance and effectiveness of designed controllers in the preceding sections are verified by implementing them on the real robot. The control structure is the same as Figure 16 for both $\mathcal{H}_\infty$ and μ controllers.

In the first scenario, the tracking performance of a circular trajectory of the closed-loop system is evaluated. Figure 22 illustrates this desired circular trajectory in the robot workspace and the tracking performance of the system using the $\mathcal{H}_\infty$ controller in the inner loop of the cascade control architecture. This path is a complete circular rotation, all of which takes about 13 seconds. In this path, the γ variable rotates about $\pm20°$ around its initial angle in $60°$. Also, rotation of the ϕ variable is about $\pm43°$ around its initial angle in $90°$ in spherical coordinates. These angles are shown in Figure 23 in order to clarify how the trajectory depicted in Figure 22 is made. The tracking error by using the designed $\mathcal{H}_\infty$ controller in the inner loop is depicted in Figure 24. Furthermore, this figure shows the tracking error by using the designed μ controller in the inner loop of the cascade control law besides a well-tuned PD controller in the outer loop, which guarantees its stability.
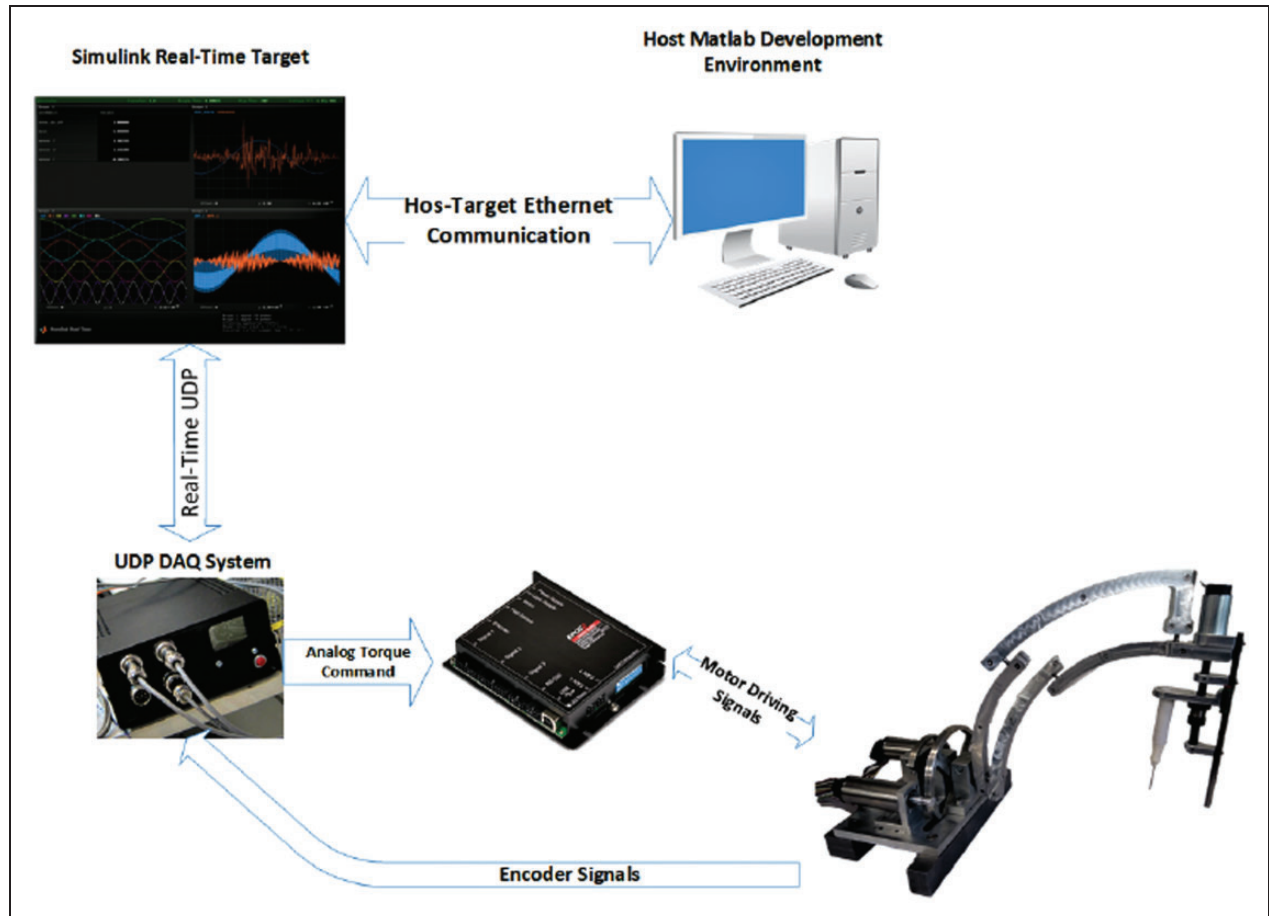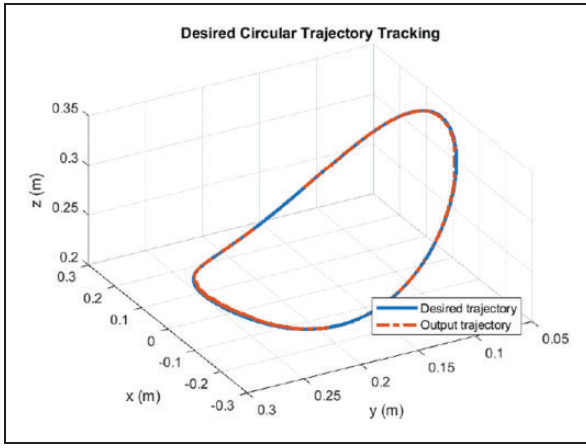

Figure 21. The overall system connections.

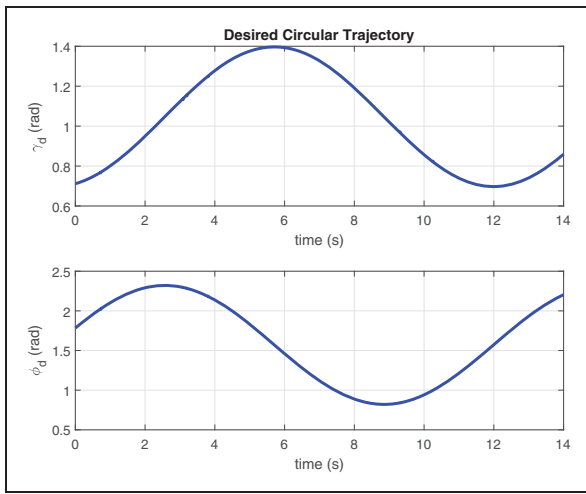**Figure 22.** Tracking performance of the desired circular trajectory using $\mathcal{H}_\infty$ controller in the inner loop.

As seen in this figure, although, tracking errors are small, obviously $\mathcal{H}_\infty$ controller has a superior performance with smaller tracking errors in practice.

On the other hand, Figure 25 shows the tracking performance of the same desired circular trajectory for a conventional well-tuned PD controller with feed-forward gravity compensation. It is clear that errors in some orientations far from the mid workspace, where PD gains are tuned, are drastically increasing. Accordingly, using the spherical to Cartesian coordinates formulation and considering that the surgery tool is in the middle of the eye, Figure 26 shows the accuracy in z-direction of the desired circular trajectory using both controllers in the inner loop in comparison with the explained PD controller. Consequently, as it can be seen, employing the cascade control structure, using robust $\mathcal{H}_\infty$-based
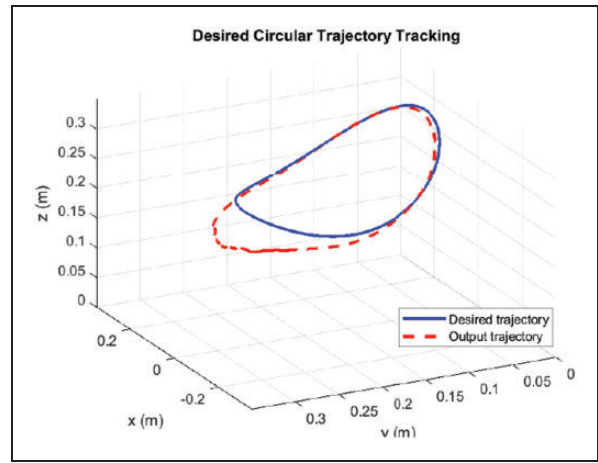

Figure 23. Desired circular trajectory shown in spherical coordinates.

Figure 25. Tracking performance of the desired circular trajectory using PD controller.
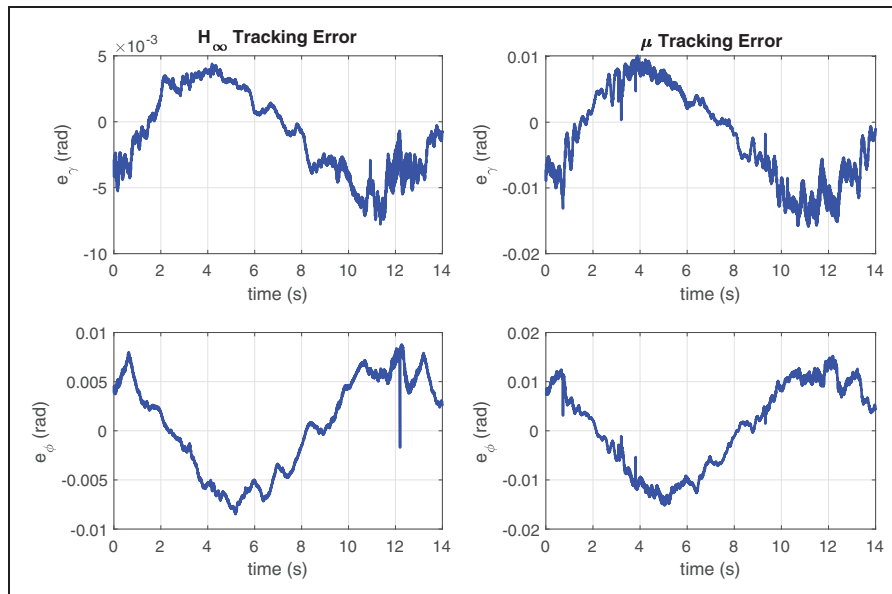

Figure 24. Tracking error of the desired circular trajectory using $\mathcal{H}_\infty$ and μ controllers in the inner loop.
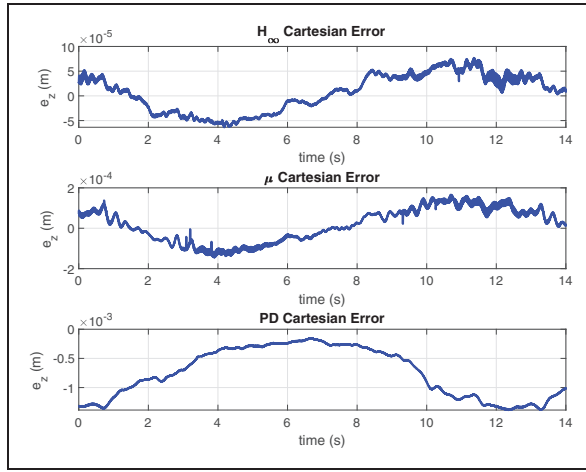
Figure 26. Accuracy in z-direction of the desired circular trajectory using H_∞ and μ controllers in the inner loop, and *PD* controller.

Table 1. Tracking errors of the desired circular trajectory for all three controllers.

RMS error	$\|e_{\mathcal{H}_\infty}\|$	$\|e_\mu\|$	$\|e_{PD}\|$
γ (rad)	0.0033	0.0074	0.087
ϕ (rad)	0.0049	0.0088	0.024

controllers, has significantly increased the tracking accuracy with a suitable stability margin in all configurations. This method is effective since the inner-loop robust controller handles complex uncertainties. The norm of tracking errors are separately shown in Table 1 for all three control strategies.

In the next experiment, we have applied some periodic pulses to the real system in different configurations. To create this trajectory, the γ variable moves from about 60° to 78°, while, the rotation of the ϕ variable is about ±30° around its initial angle 90° in every 6° movement of the γ angle in spherical coordinates. These angles are shown in Figure 27. Figure 28 illustrates this desired trajectory and the tracking performance of the system using the $\mathcal{H}_\infty$ controller in the inner loop of the cascade control architecture, while, that using the μ controller is depicted in Figure 29. From these figures, one may easily conclude that the $\mathcal{H}_\infty$ controller's performance is much better than that of the other controller. Still, for better comparison, tracking errors using each controller in the inner loop is shown in Figure 30. As expected before, the $\mathcal{H}_\infty$ controller has less oscillatory control effort that is inferred from the tracking error figure as before.

Finally, in the last experiment, we evaluate the performance of each controller in the presence of the external disturbance. For this purpose, we have added a $0.5kg$ mass to the robot end-effector, where the surgical instrument shall be placed. Then, the setpoint of γ variable is set at 70° and ϕ is set at 60°.
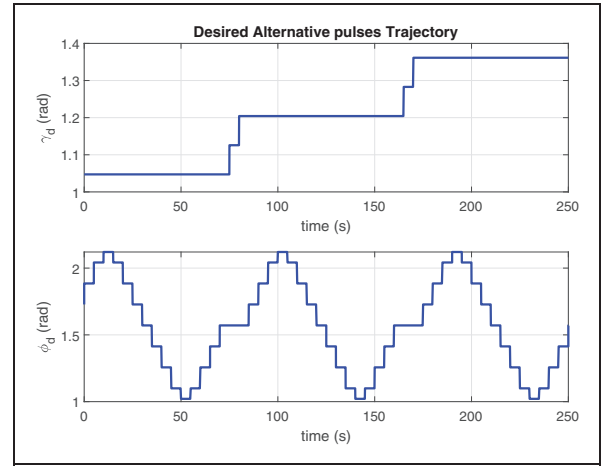

Figure 27. Desired pulses shown in spherical coordinates.

Figure 28. Tracking performance of desired pulses using $\mathcal{H}_\infty$ controller in the inner loop.
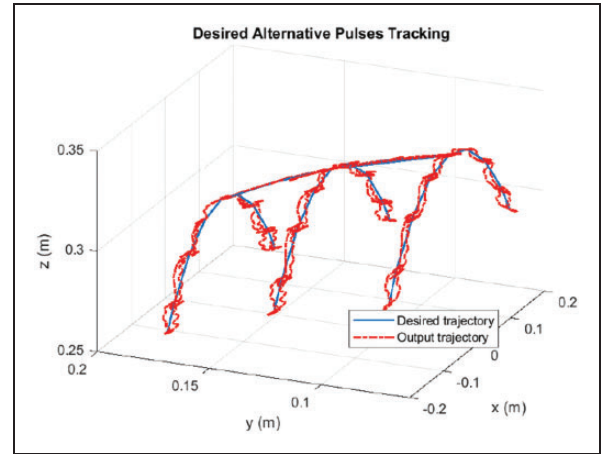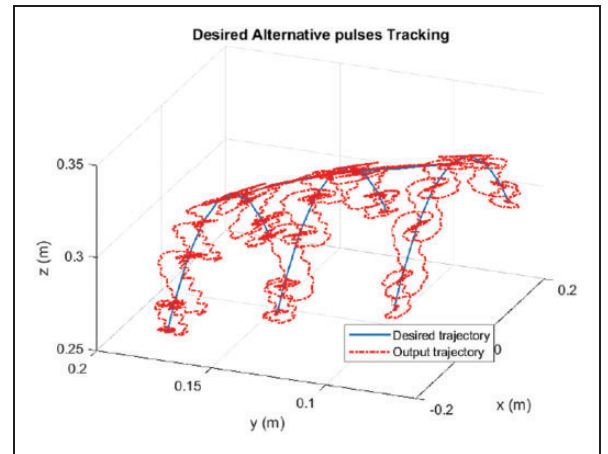

Figure 29. Tracking performance of desired pulses using μ controller in the inner loop.
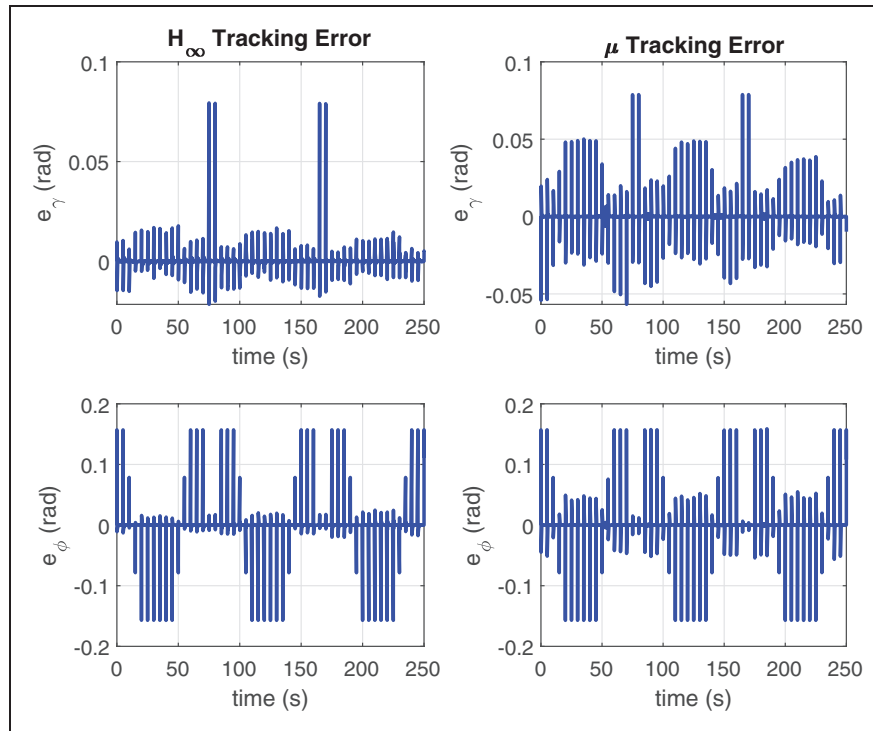
Figure 30. Tracking error of desired pulses using $\mathcal{H}_\infty$ and μ controllers in the inner loop.
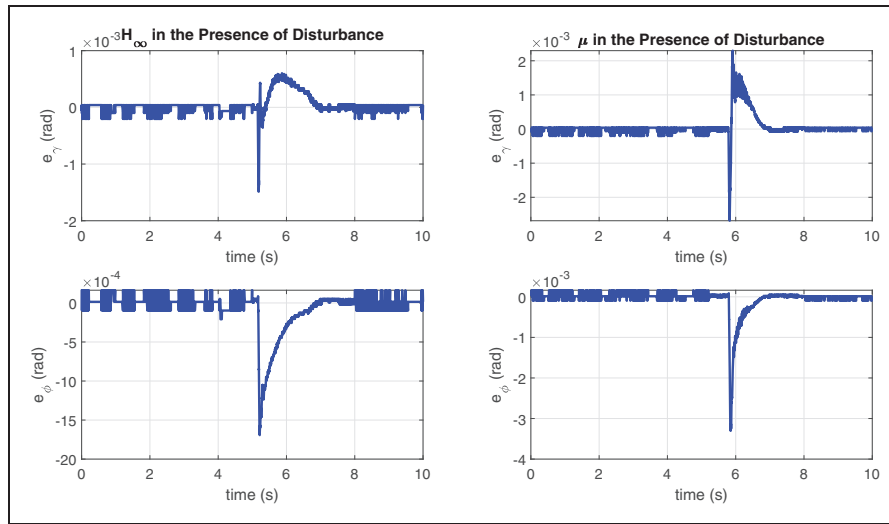

Figure 31. Regulation error in the presence of external disturbance using $\mathcal{H}_\infty$ and μ controllers in the inner loop.

After a few seconds, we have removed this payload suddenly to observe the controller behavior in disturbance rejection. Figure 31 shows the regulation error in the presence of the aforementioned external disturbance for the designed $\mathcal{H}_\infty$ and μ controllers used in the inner loop. As can be seen, the effect of disturbance in the amplitude of the $\mathcal{H}_\infty$ controller regulation error is much less than that of the μ controller. However, the μ controller has removed the disturbance effect much faster than that in the $\mathcal{H}_\infty$ controller. This is also expected since the controller gains in μ controller are higher than that in $\mathcal{H}_\infty$ one. Note that,

in all figures in this section, orientations in spherical coordinates are obtained from a forward kinematics solution taking measurements stemmed from motors' encoders as inputs.

Conclusions and future works

In this paper, we showed how much inherent uncertainties in kinematic structure and unmodeled dynamics besides external disturbances and measurement noise may influence repercussions for robot-assisted eye surgery. We then showed that applying

a cascade structure with a robust controller in the inner loop besides a stabilized well-tuned PD controller in the outer loop can reduce the effects of these uncertainties on the robot performance. For this means, the nonlinear model of the robot is encapsulated with a linear model and multiplicative uncertainty block to design robust $\mathcal{H}_\infty$ and μ-synthesis controllers for the inner loop of the cascade control structure. Then, the stability of the system as a whole was analyzed to achieve proper gains for the PD controller. Finally, we implemented three different experiments to verify the stability and performance criteria for such controllers. Results showed that the designed controllers met the stability criteria and achieved a suitable tracking performance. Although using the robust $\mathcal{H}_\infty$ controller in the velocity loop feedback was more preferable in practice. This controller shows superior performance in the presence of external noise, and periodic pulse trajectory, and in terms of repeatability and configuration independence.

Since the ARAS-Diamond robot is built to act as the slave robot in the robotic-assisted eye telesurgery system, the proposed control approach is very promising to be used for the teleoperation system. Future researches include applying the designed robust controller to a Model Mediated Teleoperation (MMT) framework, which is a very beneficial method in telesurgery applications. Besides, the whole procedure of designing controllers can be repeated by using IMU sensors in the end effector. Thus, angular feedback signals would be sensed directly from the surgical instrument movements. Hence, using designed robust controllers, one can perform real eye surgery on a phantom eye using a haptic interface to apply commands to this slave robot.

In addition, for clinical application, the robot is required to be optimized. The electrical system, for instance, will be redesigned with the controllers natively running on the ARM microcontrollers with hypervisor and fault fallback state machienes implemented. The robot's interface will modified to be user friendly, which requires advanced GUI development tools and embedded Linux systems. Finally, the robot's base will be changed ergonomically such that its setup in relation to the patient's head would be easy and safe while compatible with the required sterilizing procedures in hospitals.

Declaration of Conflicting Interests

The author(s) declared no potential conflicts of interest with respect to the research, authorship, and/or publication of this article.

Funding

Notes

a. The hinfsyn command is used.
b. Function musyn will perform this task.

References

1. Li P, Jiang S, Liang D, URL, et al. Modeling of path planning and needle steering with path tracking in anatomical soft tissues for minimally invasive surgery. *Med Eng Phys* 2017; 41: 35–45.
2. Kuo C-H and Dai J. Robotics for minimally invasive surgery: a historical review from the perspective of kinematics. In: *International symposium on history of machines and mechanisms*. Netherlands: Springer, 2009, pp.337–354.
3. Burgner-Kahrs J, Rucker DC and Choset H. Continuum robots for medical applications: a survey. *IEEE Trans Robot* 2015; 31: 1261–1280.
4. Kim C, Chung DG, Hwang M, et al. Three-degrees-of-freedom passive gravity compensation mechanism applicable to robotic arm with remote center of motion for minimally invasive surgery. *IEEE Robot Autom Lett* 2019; 4: 3473–3480.
5. Roizenblatt M, Edwards TL and Gehlbach PL. Robot-assisted vitreoretinal surgery: current perspectives. *Robot Surg* 2018; 5: 1–11.
6. Wei W, Goldman R, Simaan N, et al. Design and theoretical evaluation of micro-surgical manipulators for orbital manipulation and intraocular dexterity. In: *Proceedings 2007 IEEE international conference on robotics and automation*, Roma, 2007, pp. 3389–3395.
7. Yu H, Shen J, Joos KM, et al. Design, calibration and preliminary testing of a robotic telemanipulator for OCT guided retinal surgery. In: 2013 *IEEE international conference on robotics and automation*, Karlsruhe, 2013, pp. 225–231.
8. Taylor R, Jensen P, Whitcomb L, et al. A steady-hand robotic system for microsurgical augmentation. In: Taylor C and Colchester A (eds) *Medical image computing and computer-assisted intervention – MICCAI'99*. Berlin, Heidelberg: Springer Berlin Heidelberg, 1999, pp.1031–1041.
9. De Smet MD, Meenink TCM, Janssens T, et al. Robotic assisted cannulation of occluded retinal veins. *PLoS ONE* 2016; 11: e0162037.
10. Wilson JT, Gerber MJ, Prince SW, et al. Intraocular robotic interventional surgical system (iriss): mechanical design, evaluation, and master-slave manipulation. *Int J Med Robotics Comput Assist Surg* 2018; 14: e1842.
11. MA, Nasseri M, Maier CP and Lohmann A. Targeted drug delivery platform for assisting retinal surgeons for treating age-related macular degeneration (AMD). In: *2017 39th annual international conference of the IEEE Engineering in Medicine and Biology Society (EMBC)*, Seogwipo, 2017, pp. 4333–4338.
12. Meenink H. *Vitreo-retinal eye surgery robot: sustainable precision*. PhD thesis, Technische Universiteit Eindhoven, Department of Mechanical Engineering, 2011.
13. Wang W, Li J, Wang S, et al. System design and animal experiment study of a novel minimally invasive surgical robot: system design and animal experiments study of a MIS robot. *Int J Med Robot* 2016; 12: 73–84.

14. Li J, Wang S, Wang X, et al. Optimization of a novel mechanism a minimally invasive surgery robot, the international journal of medical robotics + computer assisted surgery. *MRCAS* 2009; 6: 83–90.

15. Ferraiuoli P, Fixsen LS, Kappler B, et al. Measurement of in vitro cardiac deformation by means of 3d digital image correlation and ultrasound 2d speckle-tracking echocardiography. *Med Eng Phys* 2019; 74: 146–152.

16. Bayatpour D, Abouali O, Ghaffarieh A, URL, et al. In silico investigation of cornea deformation during irrigation/aspiration in phacoemulsification in cataract surgery. *Med Eng Phys* 2017; 43: 77–85.

17. Hannaford B, Rosen J, Friedman DW, et al. Raven-ii: an open platform for surgical robotics research. *IEEE Trans Biomed Eng* 2013; 60: 954–959.

18. Kuo C-H, Dai J and Dasgupta P. Kinematic design considerations for minimally invasive surgical robots: an overview. *Int J Med Robot* 2012; 8: 127–145.

19. Smits J, Reynaerts D and Poorten EV. Synthesis and methodology for optimal design of a parallel remote center of motion mechanism: application to robotic eye surgery. *Mech Machine Theory* 2020; 151: 103896.

20. Ilewicz G. Multibody model of dynamics and optimization of medical robot to soft tissue surgery. In: Jablonski R and Brezina T (eds) *Advanced mechatronics solutions. Advances in intelligent systems and computing.* Cham: Springer, 2016, p.393.

21. Liu SC, Chen B and Chen L Novel linkage with remote centre of motion. In: Sung C-K and Chang J (eds) *The Fourteenth International Federation for the Promotion of Mechanism and Machine Science World Congress* (2015 IFToMM World Congress), National Taiwan University, 25–30 October 2015, pp. 1–6. Taipei Taiwan: National Taiwan University.

22. Kuo C-H and Dai JS, URL Kinematics of a fully-decoupled remote center-of-motion parallel manipulator for minimally invasive surgery. *J Med Devices* 2012; 6 021008.

23. Li J, Wang S, Wang X, et al. Development of a novel mechanism for minimally invasive surgery. In: 2010 *IEEE international conference on robotics and biomimetics*, Tianjin, 2010, pp. 1370–1375.

24. Guerrouad A and Vidal P. Smos: stereotaxical micro-telemanipulator for ocular surgery, in: Images of the twenty-first century. *Proc Annual Int Eng Med Biol Soc* 1989; 3: 879–880.

25. Baumann R, Maeder W, Glauser D, et al. The pantoscope: a spherical remote-center-of-motion parallel manipulator for force reflection. *Proc Int Conf Rob Autom* 1997; 1: 718–723.

26. Lum MJH, Rosen J, Sinanan MN, et al. Kinematic optimization of a spherical mechanism for a minimally invasive surgical robot. *IEEE Int Conf Rob Autom* 2004; 1: 829–834.

27. Schena BM and Park M. Robotic arm with five-bar spherical linkage. Patent application US8142420B2, USA, 2006.

28. Motaharifar M, Bataleblu A and Taghirad HD. Adaptive control of dual user teleoperation with time delay and dynamic uncertainty. In: 2016 24th Iranian conference on electrical engineering (ICEE), Shiraz, 2016, pp. 1318–1323.

29. Basdogan C, De S, Kim J, et al. Haptics in minimally invasive surgical simulation and training. *IEEE Comput Graph Appl* 2004; 24: 56–64.

30. Iranfar A, Motaharifar M and Taghirad HD. A dual-user teleoperated surgery training scheme based on virtual fixture. In: *2018 6th RSI international conference on robotics and mechatronics (IcRoM)*, Tehran, Iran, 2018, pp. 422–427.

31. Molaei A, Abedloo E, Taghirad HD, et al. Kinematic and workspace analysis of diamond: an innovative eye surgery robot. In: *2015 23rd Iranian conference on electrical engineering*, Tehran, Iran, 2015, pp. 882–887.

32. Danaei B, Arian A, Masouleh M, et al. Dynamic modeling and base inertial parameters determination of a 2-dof spherical parallel mechanism. *Multibody Syst Dyn* 2017; 41: 367–24.

33. Khalilpour s, Khorrambakht R, Taghirad H, et al. Robust cascade control of a deployable cable-driven robot. *Mech Syst Signal Process* 2019; 127: 513–530.

34. Rachedi M, Bouri M and Hemici B. Robust control of a parallel robot. In: *2015 international conference on advanced robotics (ICAR)*, Istanbul, 2015, pp. 428–433.

35. Qaisar T and Mahmood A. Robust control of a customized robotic arm with unstructured uncertainties. In: *2015 international conference on emerging technologies (ICET)*, Peshawar, 2015, pp. 1–5. doi:10.1109/ICET.2015.7389204.

36. Sanjeewa SD and Parnichkun M. Control of rotary double inverted pendulum system using mixed sensitivity $\mathcal{H}_\infty$ controller. *Int J Adv Rob Syst* 2019; 16: 172988141983327.

37. Seyedtabaii S. A modified fopid versus $\mathcal{H}_\infty$ and μ synthesis controllers: robustness study. *Int J Control Autom Syst* 2019; 17: 639–646.

38. Bataleblu A, Motaharifar M, Abedlu E, et al. Robust $\mathcal{H}_\infty$ control of a 2rt parallel robot for eye surgery. In: 2016 *4th international conference on robotics and mechatronics (ICROM)*, 2016, pp. 136–141.

39. Agand P, Motaharifar M and Taghirad H. Decentralized robust control for teleoperated needle insertion with uncertainty and communication delay. *Mechatronics* Tehran, 2017; 46: 46–59. doi:10.1016/j.mechatronics.2017.06.004.

40. Bolea Y, Dot P, Pujol D, et al. A parametric robust approach PID control for a laparoscopic surgery robot. *IFAC Proceedings* 2005; 38: 121–126. doi:10.3182/20050703-6-CZ-1902.01290.

41. Shu A, Deutschmann B, Dietrich A, et al. Robust $\mathcal{H}_\infty$ control of a tendon-driven elastic continuum mechanism via a systematic description of nonlinearities. *IFAC-PapersOnLine* 2018; 51: 386–392.

42. Noormohammadi-Asl A, Esrafilian O, Ahangar Arzati M, et al. System identification and $\mathcal{H}_\infty$-based control of quadrotor attitude. *Mechanical Systems and Signal Processing* 2020; 135: 106358. doi:10.1016/j.ymssp.2019.106358.

43. Taghirad HD. *Parallel robots: mechanics and control.* London; New York: Taylor & Francis, CRC Press, 2013.